Biophysical Chemistry 170 (2012) 25–33

Contents lists available at SciVerse ScienceDirect

Biophysical Chemistry

journal homepage: http://www.elsevier.com/locate/biophyschem

Ligand electronic properties modulate tau filament binding site density

Katryna Cisek, Jordan R. Jensen, Nicolette S. Honson, Kelsey N. Schafer, Grace L. Cooper, Jeff Kuret *

Department of Molecular and Cellular Biochemistry, The Ohio State University College of Medicine, Columbus, OH 43210, USA

HIGHLIGHTS

- Displacement of binding probes from synthetic tau aggregates was investigated.
- Displacement efficacy correlated with ligand polarizability.
- Polarizability increased with ligand intramolecular charge transfer efficiency.
- Ligand polarizability is a descriptor of tau-filament binding site density.

GRAPHICAL ABSTRACT

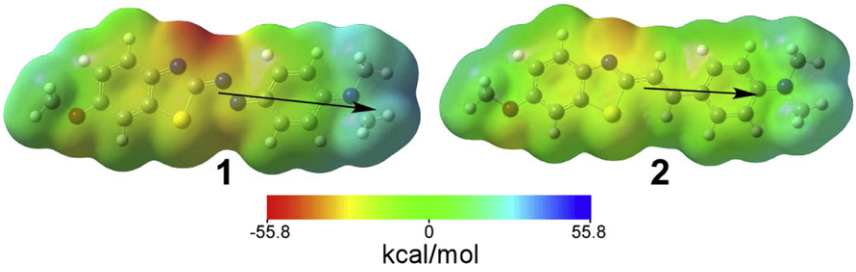

ARTICLE INFO

Article history:
Received 8 August 2012
Received in revised form 5 September 2012
Accepted 6 September 2012
Available online 11 September 2012

Keywords:
Alzheimer's disease
Tau protein
Ligand binding
Polarizability
Dispersion force
Computational chemistry

ABSTRACT

Small molecules that bind tau-bearing neurofibrillary lesions are being sought for premortem diagnosis, staging, and treatment of Alzheimer's disease and other tauopathic neurodegenerative diseases. The utility of these agents will depend on both their binding affinity and binding site density (B_{max}). Previously we identified polarizability as a descriptor of protein aggregate binding affinity. To examine its contribution to binding site density, we investigated the ability of two closely related benzothiazole derivatives ((E)-2-[[4-(dimethylamino)phenyl]azo]-6-methoxybenzothiazole) and ((E)-2-[2-[4-(dimethylamino)phenyl]ethenyl]-6-methoxybenzothiazole) that differed in polarizability to displace probes of high (Thioflavin S) and low (radiolabeled (*E*,*E*)-1-iodo-2,5-bis(3-hydroxycarbonyl-4-methoxy)styrylbenzene; IMSB) density sites. Consistent with their site densities, Thioflavin S completely displaced radiolabeled IMSB, but IMSB was incapable of displacing Thioflavin S. Although both benzothiazoles displaced the low B_{max} IMSB probe, only the highly polarizable analog displaced near saturating concentrations of the Thioflavin S probe. Quantum calculations showed that high polarizability reflected extensive pi-electron delocalization fostered by the presence of electron donating and accepting groups. These data suggest that electron delocalization promotes ligand binding at a subset of sites on tau aggregates that are present at high density, and that optimizing this aspect of ligand structure can yield tau-directed agents with superior diagnostic and therapeutic performance.

1. Introduction

Tauopathic neurodegenerative diseases, including Alzheimer's disease (AD) and certain forms of frontotemporal lobar degeneration, are characterized by the appearance of tau-aggregate bearing neurofibrillary lesions in characteristic brain regions (reviewed in Ref. [1]). The tau aggregates adopt filamentous morphology reflecting their underlying cross-β-sheet structure (*i.e.*, parallel in register β-sheets oriented perpendicular to the filament long axis) [2]. Because the spatial and temporal distribution of tau aggregates correlates with disease progression, they can be used to differentially diagnose and stage tauopathies in postmortem samples (reviewed in Ref. [3,4]). In addition to being useful biomarkers, tau aggregates are potential mediators of neurodegeneration owing to toxicity associated with their accumulation [5]. Thus, tau aggregates also are promising targets for drug discovery efforts.

To date, the search for ligands capable of binding filamentous tau aggregates has focused on affinity, resulting in the identification of

* Corresponding author at: 1060 Carmack Rd., Columbus, OH 43210. Tel.: +1 614 6885899; fax: +1 614 2925379.
E-mail address: kuret.3@osu.edu (J. Kuret).

0301-4622/$ – see front matter © 2012 Elsevier B.V. All rights reserved.
http://dx.doi.org/10.1016/j.bpc.2012.09.001

compounds with K_ds in the low- to mid-nanomolar range [6,7]. However, the utility of candidate compounds also will depend on binding site density (B_{max}). For example, the signal generated by whole-brain imaging agents is proportional to B_{avail}/K_d ratio, or "binding potential," where B_{avail} (*i.e.*, the concentration of available binding sites *in vivo*) is a function of both target concentration and B_{max} [8]. Thus, occupancy of high density sites can be important for detection of low abundance targets *in vivo*. In fact, the binding potential needed for putative tau imaging agents will likely be higher than for established amyloid radiotracers owing to the low molar concentration of the tau binding target in diseased brain relative to Aβ aggregates [9]. Ligand B_{max} also may be important for tau filament-directed therapeutics. For example, one strategy for preventing toxicity involves blocking aggregate surfaces with molecular coatings [10,11]. High B_{max} ligands would be preferable for maximizing the efficacy of this approach.

Despite its importance, little is known about binding site density on protein aggregates, except that substantial variability exists among individual ligands. For example, the presence of at least three binding modes on Aβ filaments that differ in B_{max} has been reported [12]. In the case of tau aggregates, B_{max} has been reported to vary over the range of 0.001–0.05 mol/mol (*i.e.*, 1:1000–1:20 mol ligand/mol tau protomer), suggesting that a wide range of binding site densities appear on tau filaments too [6,13,14]. Although structure activity analysis has revealed structural features on certain scaffold classes that mediate binding affinity [15,16], descriptors associated with individual modes of interaction remain poorly understood.

To better characterize the interaction between small molecules and cross-β-sheet aggregates, we have turned to benzothiazole derivatives as model ligands and quantitative structure activity relationship analysis as a means to identify their binding descriptors. Using this approach, we identified ligand polarizability as a descriptor of thioflavin dye displacement potency from synthetic cross-β-sheet aggregates composed of insulin and Aβ [17]. Polarizability, which describes how easily electron density can shift about a molecule when exposed to an external electric field, reflects underlying electron delocalization [18]. We then found that the correlation between ligand polarizability and thioflavin dye displacement potency extended to synthetic tau aggregates as well [19]. Interestingly, as thioflavin probe concentrations rose, the displacement efficacy of weakly polarizable ligands was greatly attenuated whereas the efficacy of highly polarizable ligands was unchanged [19]. These data suggested that binding site occupancy varied with probe concentration, and that ligand polarizability was a potential descriptor for binding sites occupied as probe neared saturation (corresponding to high B_{max} sites). Consistent with this possibility, an ^{18}F-labeled analog of one of most highly polarizable benzothiazole analogs in our series, (E)-4-((6-(2-(2-(2-fluoroethoxy)ethoxy)ethoxy)benzo[d]thiazol-2-yl)-diazenyl)-N, N-dimethylaniline (FPPDB), has achieved the highest B_{max} yet reported for a synthetic tau filament binding agent (~1:20 tau protomer:ligand ratio) [13].

Here we examine the relationship between ligand polarizability and site occupancy using two closely related benzothiazole derivatives as ligands, and both synthetic and authentic disease derived tau filaments as binding targets. The results indicate that incorporation of polarizability considerations into ligand design may yield agents with superior diagnostic and therapeutic performance.

2. Materials and methods

2.1. Materials

Octadecyl sulfate (ODS) was from Research Plus (Bayonne, NJ), ThT, ThS (CAS registry 1326-12-1), Congo red (ultrapure grade) was from Anaspec (Fremont, CA), and compounds **1** and **2** were custom synthesized as described [20]. Both ^{125}I-radiolabeled (in 40% ethanol) and unlabeled (*E*,*E*)-1-iodo-2,5-bis(3-hydroxycarbonyl-4-methoxy) styrylbenzene (IMSB) [21] were the generous gifts of Avid Pharmaceuticals (Philadelphia, PA).

Recombinant human His_6-2N4R tau protein was prepared as described previously [22]. Synthetic tau filaments were prepared from recombinant protein (5 μM) incubated (24 h at 37 °C) in assembly buffer (10 mM HEPES, pH 7.4, 100 mM NaCl, 5 mM dithiothreitol) in the presence of 50 μM ODS inducer [7,23], and stored in aliquots at −80 °C until used.

Authentic paired helical filament (PHF) tau was prepared from AD brain as described previously [19]. The tau content of PHF preparations was determined by dot blot using recombinant 2N4R-tau as standard. Aliquots were diluted in 0.1% SDS and 0.1% 2-mercaptoethanol, then spotted in triplicate onto 0.2 μM nitrocellulose membranes. After blocking in 4% nonfat dry milk, blots were developed using monoclonal antibody Tau5 as described previously [24]. PHF-tau weights were converted to moles assuming a mean molecular mass of 40,238 g/mol, which reflects the estimated ratios of all six human isoforms [25,26].

2.2. Filament length distributions

Filament populations were viewed and digitally captured on a Tecnai G2 Spirit BioTWIN transmission electron microscope (FEI, Hillsboro, OR) operated at 80 kV and 68,000× magnification. Filament lengths were measured using ImageJ software (National Institutes of Health) and segregated into bins as described previously [27]. Length distributions were fit to the log normal function:

$$y = ae^{\left[-0.5\left(\frac{\ln(x/x_0)}{b}\right)^2\right]} \quad (1)$$

where y is the number of filaments per bin of length interval midpoint x, a is the number of filaments per bin at distribution mode x_0, and b is an estimate of distribution skew.

2.3. Fluorescence displacement assays

ThS fluorescence assays were performed as described previously [7]. Synthetic 2N4R-tau and authentic PHF-tau filaments (1 μM total tau concentration) were incubated (2 h at 37 °C) in assembly buffer with varying concentrations of ThS probe (1.7×10^{-11}–10^{-5} M) and test ligand (0–10^{-5} M). Fluorescence was measured using a FlexStation microplate reader (Molecular Devices, Sunnyvale, CA) at λ_{ex} = 440 nm; λ_{em} = 490 nm; filter = 475 nm. Thioflavin dye displacement (net fluorescence) was determined by subtracting no protein controls from protein and compound fluorescence readings. Net fluorescence readings were normalized to percent displacement using no compound controls.

2.4. Radioligand binding assays

[^{125}I]IMSB binding and displacement from tau filaments were assessed using a filter trap assay [12,28]. Tau filaments (230 nM synthetic 2N4R-tau; 300 nM authentic PHF-tau) were incubated (4 h at 37 °C with hourly agitation) with varying concentrations of [^{125}I]IMSB and ligand in PBS buffer (10 mM Na_2HPO_4/KH_2PO_4, 137 mM NaCl, 2.7 mM KCl, pH 7.4). For determination of nonspecific binding, ligand was replaced with 8 μM of Congo red. Aliquots were then vacuum filtered (5–10 s) over glass fiber filters (0.3 μm pore diameter, Sterlitech) in a Millipore 1225 Sampling Manifold using a Pharmacia LKB VacuGene Pump operated at 50 mbar. Each sample was then washed four times with 3-ml volumes of PBS. Filters were collected in polypropylene tubes and counted using a Packard A5003 gamma counter (Packard Instrument Company, Meriden, CT) with 84% efficiency. [^{125}I]IMSB specific binding was determined by

subtracting nonspecific binding from total binding. Under these assay conditions, the specific binding signal accounted for ~80% of the total radioactivity.

2.5. Spectrophotometry

Absorbance spectra were collected in methanol solvent using a CARY50Bio UV–VIS spectrophotometer and recorded with the Cary WinUV Scan Application version 3.00(182). Spectra were fit to a double Gaussian function as described previously [29].

2.6. Analytical methods

Binding and displacement potencies of ligands in radioactivity and fluorescence assay formats were determined from the function:

$$F = F_{\min} + \frac{F_{\max} - F_{\min}}{1 + (x/AC_{50})^n} \quad (2)$$

For direct binding assays, F represents the net signal at concentration x of probe, $F_{\min}$ is the signal at zero probe concentration, $F_{\max}$ is the net signal at infinite probe concentration, n is the Hill coefficient, and AC_{50} corresponds to probe K_d. For displacement assays conducted at constant probe concentration, F represents the probe signal in the presence of varying concentrations of test ligand, $F_{\min}$ is the signal at infinite ligand concentration, $F_{\max}$ is the signal in the absence of test ligand, AC_{50} is the concentration of test compound that reduces probe signal by 50%.

2.7. Computational chemistry

Quantum property calculations were performed using density functional theory methods implemented in Gaussian 09 (G09) [30] and Turbomole V6.3.1 [31] software packages available on Ohio Supercomputer Center clusters. All calculations were performed using hybrid density functional B3LYP and the 6-311++G(d,p) basis set, which together have been reported to accurately model photophysical properties of dye molecules in implicit solvent [32].

Dipole moments were calculated in G09 after optimizing ground state geometries using G09 as described previously [17] and excited state calculations for λ_{max} were performed using time-dependent density functional theory (TD-DFT) method (G09 keyword TD = NStates = 3). Electrostatic potential surface calculations were performed on compound ground-state geometries using population analysis with atomic charge assignments produced according to the ChelpG scheme [33] (G09 keyword pop = chelpg) as implemented in G09. Surface plots were generated in GaussView 4.1.2 by mapping electrostatic potentials onto SCF (self consistent field) total density surfaces with isodensity contour values of ±0.0004 a.u. To facilitate direct comparison between compounds, electrostatic potential energy scales were normalized to a standard color scale (±55.8 kcal/mol) such that all potentials resided within the standard extremes. For all G09 calculations, bulk solvent effects were implicitly modeled with the polarizable continuum model [34] (G09 keywords SCRF = (Solvent = Methanol)).

Electronic difference density calculations were performed in Turbomole for first excited (S_1) and ground states (S_0) on compound ground-state geometries under C_1 molecule symmetry (control keywords $scfinstab and $soes) as implemented in the Turbomole egrad module. Because this module does not implement implicit solvent effects, these calculations were performed in gas phase. Electronic difference maps were generated using UCSF Chimera Alpha Version 1.5 (build 31329) [35] software with isodensity contour values ±0.004 a.u. Contour volumes were measured using Chimera's Volume tool.

The calculated log octanol/water partition coefficient (clogP) and molecular volume were calculated with the Molinspiration Property Calculation Service (www.molinspiration.com).

3. Results

3.1. Tau filament populations for binding studies

Synthetic filaments composed of recombinant 2N4R-tau were prepared to investigate ligand binding properties. The 2N4R isoform was chosen because it efficiently aggregates *in vitro* and has been used in previous investigations of ligand binding [7,13,19]. Tau filaments prepared from AD brain also were prepared so that interaction with authentic aggregates could be compared. These filaments differed from synthetic filaments by being composed of all six central nervous system isoforms and by containing extensive post-translational modifications (reviewed in Ref. [1]). Both preparations displayed clear filamentous character when viewed in transmission electron micrographs (Fig. 1A,B). However, they differed in morphology, with synthetic filaments displaying straight morphology whereas the authentic filaments retained the classic morphology of PHF (Fig. 1A,B). Moreover, the two filament populations differed in length distribution. The PHF population averaged 193 nm in length and displayed a clear mode at 123 ± 2 nm when fit to a log-normal distribution (Fig. 1C). These dimensions, which were consistent with literature values for filaments isolated by differential centrifugation [36], reflect the effects of breakage and shearing during isolation. In contrast, synthetic 2N4R-tau filaments averaged 776 nm in length and were predicted on the basis of a log-normal distribution to have a mode within the standard error of estimate of zero (Fig. 1C). These data indicate that synthetic filament length distribution was skewed toward longer lengths relative to PHFs.

3.2. Displacement probes

To characterize the binding surfaces presented by tau filaments, the interaction of each filament preparation with fluorescent thioflavin dyes (ThT and ThS) [37] and radioprobe [^{125}I]IMSB [21] was investigated. These compounds were chosen as binding probes because they had been reported to bind tau-bearing neurofibrillary lesions in brain sections [38,39] yet differed substantially in structure. For example, the major component of ThS adopts a donor-π-acceptor (D-π-A) configuration, composed of strong benzothiazolium electron acceptors linked to a strong dimethylamine electron donor through a planar conjugated π network (Table 1). In contrast, IMSB has two weak methoxy electron donors feeding into a conjugated aromatic π network yielding a donor-π-donor (D-π-D) configuration (Table 1). As a result, ThS was a colored compound with a strong absorbance maximum at 377 nm and a weak shoulder at 420 nm, whereas IMSB appeared colorless with an absorbance maximum centered at 350 nm (Fig. 2). Overall, ThS and IMSB probes were charged molecules of similar size and shared planar, highly conjugated organization (Table 1). However, they differed in hydrophobicity and electronic structure, especially in the magnitude of delocalization of their π electron systems.

When assayed in filter trap format (300 nm pore diameter) at constant tau protomer concentration, both 2N4R aggregates and PHF-tau bound [^{125}I]IMSB with affinities estimated in the low nanomolar range (Fig. 3A). However, B_{max} was only 1:112 ± 25 ([^{125}I]IMSB:tau) for 2N4R tau and 1:2990 ± 160 ([^{125}I]IMSB:tau) for PHF. Because the percentage of total aggregation distributed into filaments ≥300 nm in length was higher for synthetic filaments (90%, Fig. 1C) than for PHFs (31%, Fig. 1C), a portion of the observed B_{max} difference may have resulted from differences in filament length distribution. However, the majority of the 23 ± 2 fold difference in B_{max} reflected a lower density of high affinity IMSB sites on PHFs relative to synthetic filaments.

When synthetic filaments were assayed in fluorescence format with near saturating concentrations of ThS and ThT, both probes underwent excitation and emission Stokes shifts and fluoresced brightly (Fig. 3B). These results were consistent with previous reports [40]. However, only ThS fluoresced strongly in the presence of PHF,

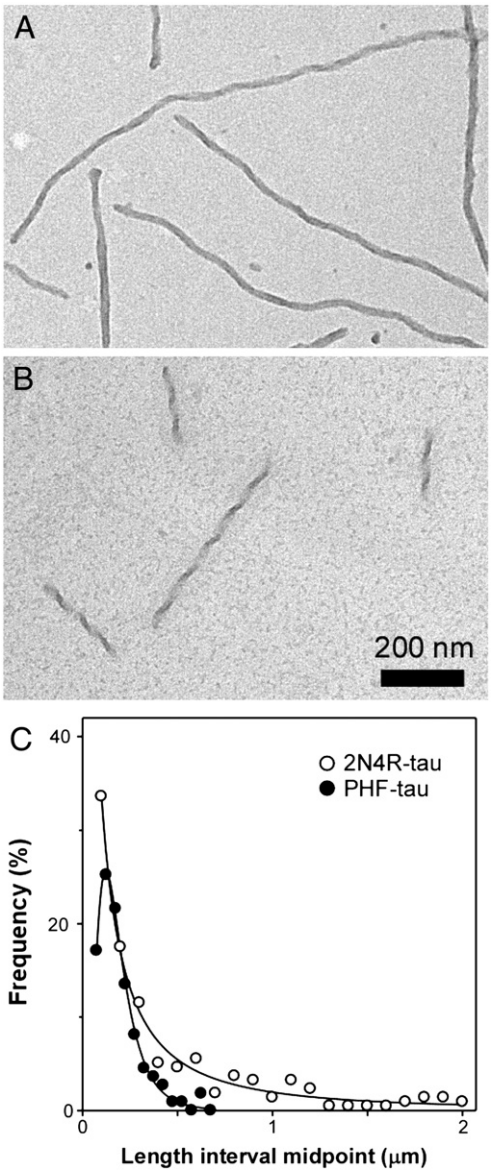

Fig. 1. Tau filament morphology and length distribution. Transmission electron microscope images of negatively stained A, synthetic filaments composed of 2N4R-tau and B, authentic tau filaments purified from AD brain were captured at 68,000-fold magnification. Synthetic filaments adopted straight morphology, whereas authentic filaments adopted classic paired helical morphology. C, the dimensions of all filaments ≥50 nm in length measured from electron micrographs were plotted as the fraction of total filament number that segregated into consecutive length intervals (total filament number $n = 247$ and 111 for 2N4R- and PHF-tau, respectively), whereas each line represents the best fit of data points to a log normal function (Eq. (1)). The length distribution of synthetic 2N4R filaments skewed toward longer lengths relative to the PHF population.

with ThT fluorescence intensity being 15 ± 1 fold lower than in the presence of equimolar concentrations of 2N4R filament protomer (Fig. 3B). To maintain tau protomer concentrations at similar levels for interaction assays involving synthetic and authentic filaments, all subsequent studies involving thioflavin dye probes used ThS exclusively.

To clarify the relationship between IMSB and ThS sites, the ability of probes to displace each other was investigated. Despite its high binding affinity, IMSB proved incapable of displacing ThS from either synthetic tau filaments (Fig. 4A) or authentic PHF-tau (Fig. 4B) by 50% when present at saturating concentrations up to 10 μM. In contrast, ThS completely displaced [^{125}I]IMSB from synthetic filaments with AC_{50} of 249 ± 60 nM (Fig. 5). Together these data indicated that IMSB and ThS differentially interacted with tau filaments, with IMSB selectively probing low density sites capable of supporting high affinity binding. In contrast, ThS interacted with IMSB sites but also additional sites that were present at similar densities on both PHF and synthetic filaments.

3.3. Benzothiazole ligands differentially displace IMSB and ThS probes

To further characterize IMSB and ThS modes of interaction, the ability of neutral benzothiazole derivatives **1** and **2** (Table 1) to displace each probe was investigated. The two ligands differed only by the structure of the bridge that connected the benzothiazole and aryl moieties: **1** contained an azo bridge whereas **2** contained an alkene bridge. As a result, the two compounds shared similar size, hydrophobicity and neutral net charge (Table 1). Nonetheless, bridge structure greatly affected compound absorbance, with compound **1** appearing red and having an intense lowest energy charge-transfer absorption band centered at 508 nm whereas **2** appeared yellow and absorbed at 393 nm (Fig. 2B). Consistent with previous results [20], **1** efficiently displaced ThS probe from synthetic 2N4R filaments with an AC_{50} of 31 ± 6 nM (Fig. 4A). In contrast, **2** did not displace ThS by 50% at concentrations up to 10 μM. A similar pattern was observed for ThS displacement from PHF, where **1** displaced ThS with AC_{50} of 48 ± 4 nM and **2** displaced with $AC_{50} > 10$ μM (Fig. 4B). These data indicate that **1** had far greater ability than **2** to interact with binding sites occupied by ThS, and that this pattern of interaction held for authentic PHFs as well as for synthetic filaments.

On the basis of ThS probe displacement described above, compound **2** appeared to bind poorly to tau filaments. Yet when tested in [^{125}I]IMSB competition format, **1** and **2** both displaced probe with similar affinity (AC_{50}s of 29 ± 6 and 45 ± 11 nM, respectively), and with nearly equal efficacy (Fig. 5). These data reveal that both **1** and **2** were capable of binding tau filaments with high affinity at the low density sites bound by IMSB, but that they differed greatly in their ability to bind the additional sites occupied by near saturating concentrations of ThS probe.

3.4. Electronic properties of tau aggregate binding ligands

To characterize their electronic properties, the *E* geometric isomers of **1** and **2** (shown in Table 1) were analyzed using a quantum chemical modeling approach. First, the ground state geometries of **1** and **2** were optimized in polar solvent at the B3LYP/6-311++G(d,p) level of theory. To test the quality of the models, λ_{max} and oscillator strength corresponding to vertical excitations S_1, S_2, and S_3 were calculated and compared to experimental values. The calculations predicted that the S_1 state far exceeded S_2 and S_3 in oscillator strength for both compounds (Table 2). Indeed, experimental values for λ_{max} were in general agreement with values calculated for the $S_0 \rightarrow S_1$ excitation for both compounds (Table 2). However, λ_{max} for **2** was slightly overestimated in the calculation, potentially reflecting greater rotational freedom of its dimethylamine moiety [41,42].

Second, to assess overall compound polarity in the ground state, calculated molecular electrostatic surface potentials were mapped onto electron density isosurfaces and plotted along with dipole moment. Both compounds presented electronegative surfaces along the faces of their conjugated π systems (Fig. 6A). However, for compound **1**, negative electrostatic potential localized most intensely on the nitrogen atoms of the benzothiazole heterocycle and azo bridge, with positive electrostatic potential localized primarily on the dimethylamine electron donor group. This pattern was consistent with extensive delocalization of electrons through the conjugated π system from donor groups toward thiazole and azo group nitrogen atoms. The resulting separation of negative and positive charges created a permanent ground state dipole moment of 7.8 D oriented approximately parallel to the compound long axis (Fig. 6A). In

Table 1
Compound structures and characteristics.

Compound	Structure[a]	MW	λ_{max} (nm)	clogP	Volume (Å^3)
Probes					
ThS	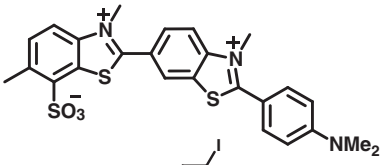	493	377	−4.3	427
IMSB	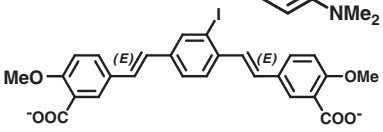	554	350	3.7	418
Ligands					
1	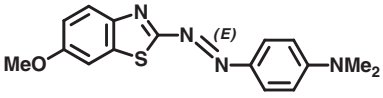	310	508	4.8	277
2	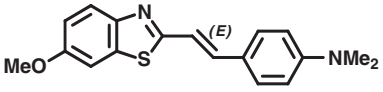	312	393	4.6	285

[a] ThS is a mixture of substances [37]. The chemical structures of its major components are available in the PubChem Substance and Compound database through substance identifier number SID: 8137049 and/or unique chemical structure identifier CID: 415676 [52].

contrast, compound **2** supported lower charge polarity, with localized negative charge being limited to the nitrogen atom of the benzothiazole moiety (Fig. 6A). As a result, ground state dipole moment decreased 30% relative to **1**. These data indicate that the azo bridge fostered more effective coupling between electron donor and acceptor groups than the alkene bridge, resulting in more charge transfer character in the ground state of **1** relative to **2** in polar solvent. Proposed resonance forms that contribute to charge transfer character are shown in Fig. 6B.

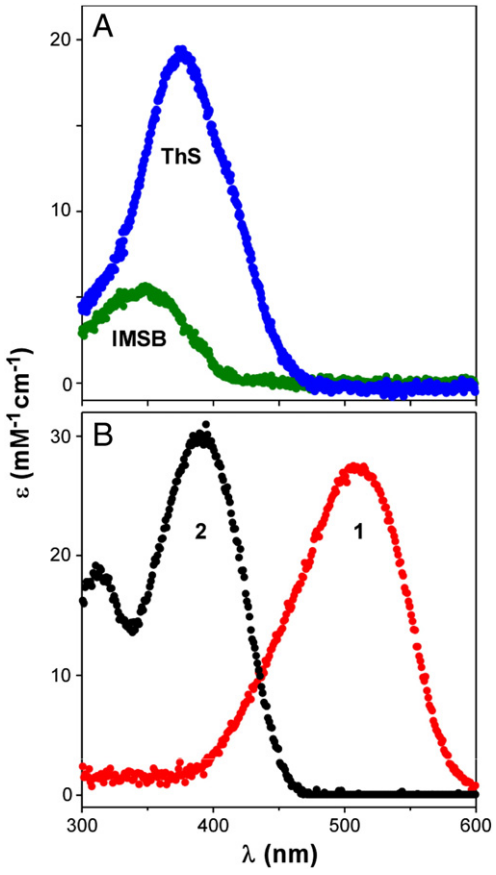

Fig. 2. Optical properties of probes and ligands. Experimental absorption spectra for A, probes ThS and IMSB and B, ligands **1** and **2** were determined in methanol solvent. Each point represents absorbance normalized for cuvette pathlength and compound concentration (*i.e.*, extinction coefficient) plotted as a function of wavelength (λ). See text for details.

Finally, to model how bridge composition affected electron movement to higher energy states, vertical excitations were calculated for **1** and **2** at the B3LYP/6-311++G(d,p) level of theory and used to compute differences in electron density between the ground (S_0) and lowest identified singlet excited states (S_1). Analysis was limited to gas phase owing to computational constraints. The resultant S_1–S_0 difference maps identified the locations of electron density that dispersed from the ground state and accumulated upon excitation to the higher energy level (Fig. 7). The S_1–S_0 difference density map for **2** exhibited a change in electron density that alternated in sign along the conjugated alkene bridge, which is characteristic of a (π, π^*) excited state. Electron density on the methoxy and dimethylamine donors shifted further toward the thiazole ring in the excited state. In contrast, the S_1–S_0 difference density map for **1** was dominated by the depletion of electron density from the lone pairs of the bridge nitrogen atoms, implicating a (n, π^*) excited state. Electron density redistributed toward the thiazole and phenyl ring systems and within the bridge. Overall, the difference maps showed that the volume of perturbed density was 1.7-fold greater for **1** relative to **2** (on the basis of identical isocontouring), consistent with increased charge transfer efficiency in this compound. Together these calculations show that simple replacement of the alkene bridge in **2** with an azo moiety to create **1** altered compound electronic properties by enhancing electron delocalization in the ground state and by supporting greater intramolecular charge transfer in response to photoexcitation. These characteristics, which were fostered while holding compound hydrophobicity, size, and net charge nearly constant, correlated with increased displacement efficacy against sites occupied by ThS probe relative to those occupied by the IMSB probe.

4. Discussion

These data show that the efficacy of probe displacement from tau filaments is highly sensitive to the electronic properties of ligand.

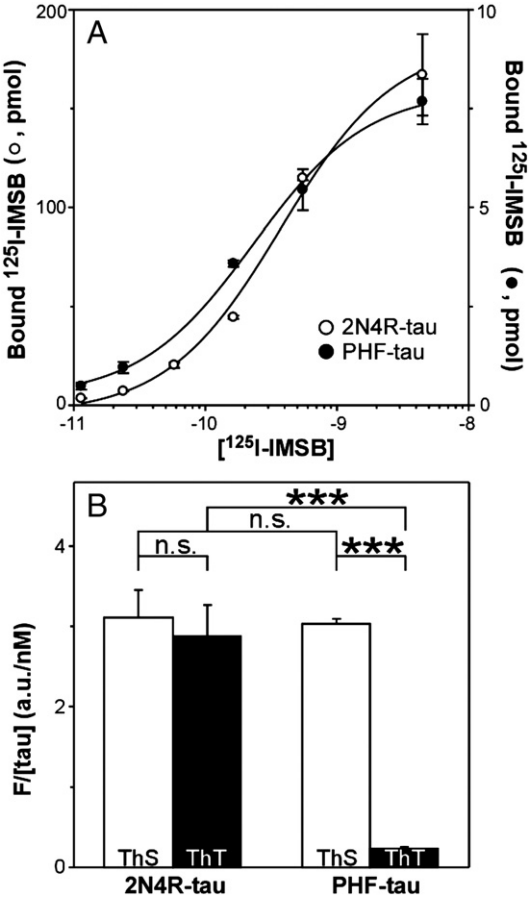

Fig. 3. Probe interactions with filamentous 2N4R- and PHF-tau. A, binding of radioprobe [^{125}I]IMSB was determined after incubation with synthetic and paired helical tau filaments. Each point represents specific binding as a function of total [^{125}I]IMSB concentration ± SD (triplicate determination), whereas the lines represent the best fit of the data points to a binding isotherm (Eq. (2)). [^{125}I]IMSB bound to both synthetic and paired helical filaments with low nanomolar affinity. ***, $p<0.001$; n.s., $p>0.05$ for each comparison. B, probes ThS (7.5 μM) and ThT (1 μM) were incubated with tau filaments composed of 2N4R- and PHF-tau (each at 1 μM), then subjected to fluorescence measurements at $\lambda_{ex}=440$ nm, $\lambda_{em}=490$ nm. Each bar represents net fluorescence yield associated with binding ± SD (triplicate determination). ThS fluoresced strongly in the presence of both 2N4R filaments and PHFs, whereas ThT fluoresced most strongly in the presence of 2N4R filaments.

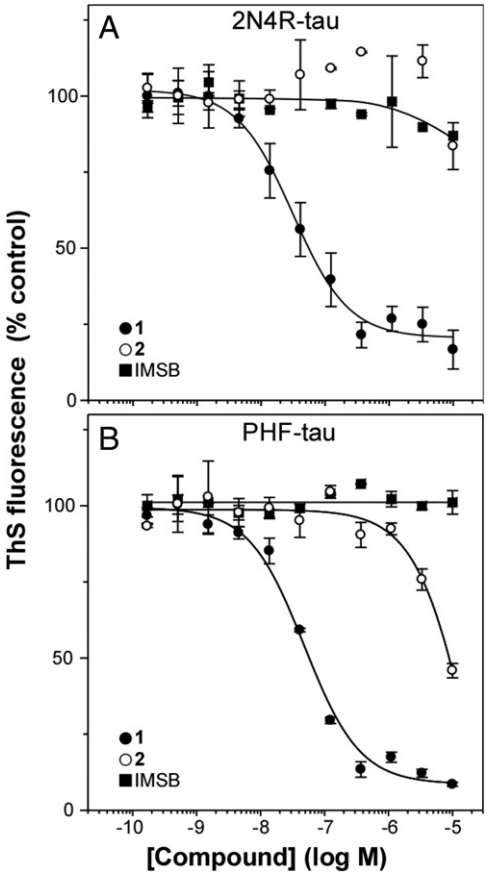

Fig. 4. ThS displacement assays for tau filament binding. A, synthetic 2N4R-tau filaments and B, PHFs (both at 1 μM) were incubated with fluorescent ThS probe (7.5 μM) in the presence of varying concentrations of **1**, **2**, and unlabeled IMSB, then subjected to fluorescence measurements at $\lambda_{ex}=440$ nm, $\lambda_{em}=490$ nm. Each point represents mean net ThS fluorescence (F) (expressed as % fluorescence in the presence of vehicle alone) whereas the solid lines reflect best fit of data points to Eq. (2). Only compound **1** decreased ThS fluorescence from both filament populations at submicromolar concentrations under these conditions.

Importantly, they show that displacement of near saturating concentrations of ThS probe, which occupies sites over and above those occupied by IMSB, can be selectively enhanced by fostering a highly delocalized electronic structure. Thus, they suggest a route for rationally maximizing the binding potential of imaging radiotracers and the efficacy of interaction-inhibiting molecular coatings [10,11]. Because PHF-tau shares this behavior with synthetic 2N4R-tau filaments, the route can yield ligands with utility for human disease. Because electronic properties can be modulated in small molecules while maintaining zero net charge, the proposed strategy is consistent with the need to maintain blood brain barrier penetrability of ligands for diagnostic and therapeutic applications.

A role for electronic structure in mediating filament binding is consistent with recent models of small molecule/cross-β-sheet aggregate interactions formulated on the basis of docking [43,44] and molecular dynamics simulation [45–47]. These computational models predict that binding occurs in shallow channels oriented parallel to the long filament axis formed by solvent exposed amino acid side chains. Thus, potential binding sites are predicted to vary with the dimensions of the channels and their surface chemical properties (*e.g.*, amino acid side chain composition). The most energetically favorable interactions identified involved Phe residues, which presented a surface composed of aromatic moieties, and Gly residues, which exposed the delocalized π system of the cross-β-sheet main chain core [44,46]. In the case of compounds investigated herein, two modes of binding with tau aggregates could be discerned. The first mode, which we call Class I, is characterized by high affinity but low B_{max} binding. Class I activity is shared by diverse structures composed of planar and highly conjugated ring systems that present π-electron rich surfaces, including all four of the probes and ligands investigated herein. Their π-electron systems can but need not be highly delocalized, and as a result these compounds are frequently colorless (*e.g.*, IMSB). The location of their binding sites on tau aggregates is not established, but π-rich heterocycles have been reported to support cation-π, π-π, and CH-π interactions (reviewed in Ref. [48]). A tau-aggregate directed radiotracer with Class I electronic character currently undergoing clinical development, THK523 [6], shares a D-π-D electronic organization with IMSB. Although it binds synthetic tau aggregates with a low nanomolar K_d, its B_{max} is only 0.002 mol/mol (*i.e.*, one ligand molecule for every 460 tau protomers). This binding site density is within ~4-fold of IMSB, but >20-fold lower than FPPDP, an analog of **1**. On the basis of mathematical modeling, we have predicted that this combination of binding parameters (*i.e.*, binding potential) will have difficulty overcoming nonspecific background associated with whole-brain imaging [9]. Imaging performance will be weaker still if, as shown here for [^{125}I]IMSB, B_{max} for authentic PHF is lower than for synthetic tau filaments.

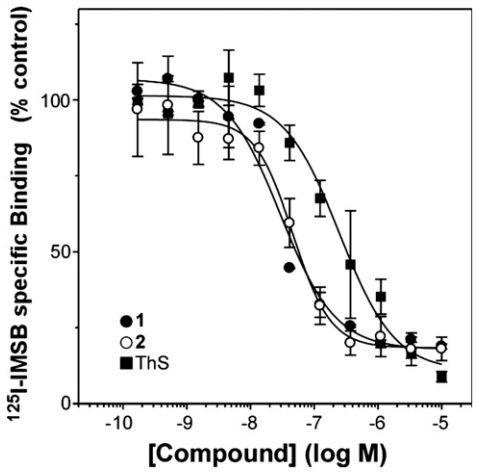

Fig. 5. [^{125}I]IMSB displacement assays for tau filament binding. Binding of radioprobe [^{125}I]IMSB to synthetic 2N4R-tau filaments (1 μM) was determined after incubation in presence of varying concentrations of **1**, **2**, and ThS. Each point represents specific binding (expressed as % specific binding in the presence of vehicle alone) as a function of total ligand concentration ± range (duplicate determination), whereas the lines represent the best fit of the data points to Eq. (2). All three compounds displaced [^{125}I]IMSB specific binding under these conditions.

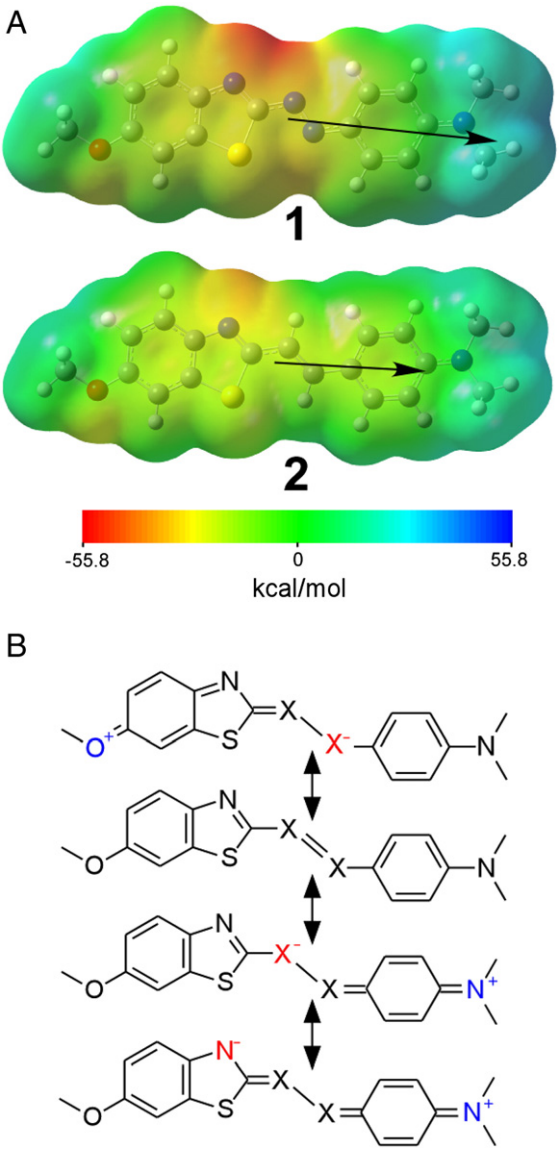

Fig. 6. Ligand electrostatic potential surfaces. A, plots for **1** and **2** were generated at the B3LYP/6-311++G(d,p) level of theory and visualized in GaussView 4.1.2. The semi-transparent electrostatic potential surface, color-coded red (−55.8 kcal/mol) to blue (55.8 kcal/mol), overlays compound ball and stick atoms (carbon, grey; hydrogen, white; nitrogen, blue; oxygen, red; and sulfur, yellow). Calculated dipole moments are depicted as arrows. B, neutral and charge transfer resonance forms, where X = C or N. See text for details.

In contrast, the second binding mode, which we term Class II, is shared by compounds comprising planar and highly conjugated π systems flanked by electron donor and acceptor groups [19]. As a result, these compounds, which can be intensely colored (*e.g.*, compound **1**), have more highly delocalized electrons in the ground state and greater electron mobility in response to photoexcitation than Class I compounds. These electronic characteristics are ideal for supporting attractive van der Waals interactions with flat binding surfaces on tau and other protein aggregates (reviewed in Ref. [49]). Conversely, Class I compounds lack this feature and displace Class II ligands poorly. We propose that this mode of interaction is responsible for the high binding site densities associated with a radiolabeled derivative of **1** [13], which was reported to bind synthetic tau aggregates with B_{max} up to one order of magnitude greater than Class I compounds [^{125}I]IMSB (reported herein) or [^{18}F]THK523 [6]. On the basis of mathematical modeling, we predict that this B_{max} (when accompanied by low nanomolar affinity) is adequate for whole-brain imaging applications [9]. Moreover, we have reported that compound **1**, but not **2**, is capable of blocking toxicity associated with tau aggregation in a biological model of tauopathy [50]. Together these data suggest that the Class II mode of interaction offers translational opportunities for tauopathic neurodegenerative diseases.

Our reported quantitative structure activity relationship analysis of benzothiazole derivatives [17], along with quantum chemistry analysis of compounds **1** and **2** reported herein, provide insight into the structural features associated with Class II activity. The most important feature is the introduction of electron acceptor and donor moieties that foster electron delocalization. In the case of **1**, this was achieved by placing an azo bridge adjacent to the weak benzothiazole acceptor in a conjugated π system flanked by electron donating groups. The resulting D-π-A-π-D architecture strongly enhanced intramolecular charge transfer, leading to extensive π electron delocalization in the ground state and lower energy requirements for transition to the first excited state. The resulting increase in dipole moment and polarizability in **1** relative to **2** reflect these features. The dispersion effects supported by this architecture may be especially important for high density binding to tau aggregates, which contain multiple Gly and aromatic residues in their folded core [51]. Nonetheless, compound **1** does not discriminate between Aβ and tau on the basis of ThS displacement activity [7], and this has been confirmed by direct radiobinding assays [13]. It remains to be seen whether Class II interactions can be harnessed to drive selectivity among protein aggregates composed of different protein protomers.

Table 2
Calculated (cal) and experimental (exp) absorbance bands for **1** and **2**.[a]

Compound:	1		2	
State	λ_{cal}[b] (nm)	λ_{exp} (nm)	λ_{cal}[b] (nm)	λ_{exp} (nm)
S_1	493 (1.51)	508	428 (1.57)	393
S_2	460 (0.00)	–	330 (0.05)	–
S_3	395 (0.01)	–	311 (0.04)	310

[a] Values in parentheses represent calculated oscillator strengths.
[b] Calculated in implicit methanol solvent.

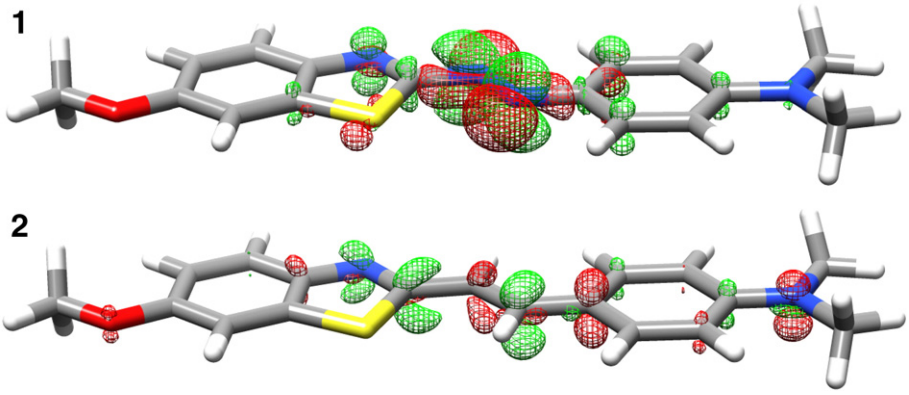

Fig. 7. Ligand electronic difference density maps. Plots for **1** and **2** were generated at the B3LYP/6-311++G(d,p) level of theory and visualized in UCSF Chimera Alpha Version 1.5 (build 31329) with isocountour values normalized to ±0.004 a.u. Green contours represent the accumulation of electron density in the S_1 excited state whereas red contours depict the loss of electron density from the S_0 ground state. Atom colors represent carbon (gray), hydrogen (white), nitrogen (blue), oxygen (red), and sulfur (yellow). See text for details.

In summary, here we found that highly delocalized electronic structure fostered potent displacement of cross-β-sheet binding probes from tau aggregates, but only from a subset of binding sites marked by near-saturating concentrations of ThS probe. The high density nature of the sites, combined with the compatibility of delocalized electronic structure with overall neutral compound charge, suggests a route for optimization of binding properties for diagnostic and therapeutic applications.

Acknowledgments

We thank Drs. Christopher M. Hadad and Shubham Vyas (The Ohio State University, Columbus, OH) for helpful discussions on quantum chemistry theory and practice, Dr. Seok Rye Choi (Avid Radiopharmaceuticals, Philadelphia, PA) for her gift of [^{125}I]IMSB, and Drs. Dennis B. McKay and Erich Grotewold (The Ohio State University, Columbus, OH) for access to spectroscopy resources. This work was supported by a grant from the Alzheimer's Drug Discovery Foundation (281205) and an allocation of computing time from the Ohio Supercomputer Center (PAS0453).

References

[1] N. Sergeant, A. Bretteville, M. Hamdane, M.L. Caillet-Boudin, P. Grognet, S. Bombois, D. Blum, A. Delacourte, F. Pasquier, E. Vanmechelen, S. Schraen-Maschke, L. Buee, Biochemistry of Tau in Alzheimer's disease and related neurological disorders, Expert Review of Proteomics 5 (2008) 207–224.
[2] M.R. Sawaya, S. Sambashivan, R. Nelson, M.I. Ivanova, S.A. Sievers, M.I. Apostol, M.J. Thompson, M. Balbirnie, J.J. Wiltzius, H.T. McFarlane, A.O. Madsen, C. Riekel, D. Eisenberg, Atomic structures of amyloid cross-β spines reveal varied steric zippers, Nature 447 (2007) 453–457.
[3] H. Braak, E. Braak, Staging of Alzheimer's disease-related neurofibrillary changes, Neurobiology of Aging 16 (1995) 271–278 discussion 278–284.
[4] M.B. Feany, D.W. Dickson, Neurodegenerative disorders with extensive tau pathology: a comparative study and review, Annals of Neurology 40 (1996) 139–148.
[5] M.M. Mocanu, A. Nissen, K. Eckermann, I. Khlistunova, J. Biernat, D. Drexler, O. Petrova, K. Schonig, H. Bujard, E. Mandelkow, L. Zhou, G. Rune, E.M. Mandelkow, The potential for β-structure in the repeat domain of tau protein determines aggregation, synaptic decay, neuronal loss, and coassembly with endogenous Tau in inducible mouse models of tauopathy, Journal of Neuroscience 28 (2008) 737–748.
[6] M.T. Fodero-Tavoletti, N. Okamura, S. Furumoto, R.S. Mulligan, A.R. Connor, C.A. McLean, D. Cao, A. Rigopoulos, G.A. Cartwright, G. O'Keefe, S. Gong, P.A. Adlard, K.J. Barnham, C.C. Rowe, C.L. Masters, Y. Kudo, R. Cappai, K. Yanai, V.L. Villemagne, ^{18}F-THK523: a novel *in vivo* tau imaging ligand for Alzheimer's disease, Brain 134 (2011) 1089–1100.
[7] N.S. Honson, R.L. Johnson, W. Huang, J. Inglese, C.P. Austin, J. Kuret, Differentiating Alzheimer disease-associated aggregates with small molecules, Neurobiology of Disease 363 (2007) 229–234.
[8] M. Laruelle, M. Slifstein, Y. Huang, Relationships between radiotracer properties and image quality in molecular imaging of the brain with positron emission tomography, Molecular Imaging and Biology 5 (2003) 363–375.
[9] K.N. Schafer, S. Kim, A. Matzavinos, J. Kuret, Selectivity requirements for diagnostic imaging of neurofibrillary lesions in Alzheimer's disease: a simulation study, NeuroImage 60 (2012) 1724–1733.
[10] L.K. Habib, M.T. Lee, J. Yang, Inhibitors of catalase-amyloid interactions protect cells from beta-amyloid-induced oxidative stress and toxicity, Journal of Biological Chemistry 285 (2010) 38933–38943.
[11] P. Inbar, J. Yang, Inhibiting protein-amyloid interactions with small molecules: a surface chemistry approach, Bioorganic & Medicinal Chemistry Letters 16 (2006) 1076–1079.
[12] A. Lockhart, L. Ye, D.B. Judd, A.T. Merritt, P.N. Lowe, J.L. Morgenstern, G. Hong, A.D. Gee, J. Brown, Evidence for the presence of three distinct binding sites for the thioflavin T class of Alzheimer's disease PET imaging agents on β-amyloid peptide fibrils, Journal of Biological Chemistry 280 (2005) 7677–7684.
[13] K. Matsumura, M. Ono, H. Kimura, M. Ueda, Y. Nakamoto, K. Togashi, Y. Okamoto, M. Ihara, R. Takahashi, H. Saji, ^{18}F-labeled phenyldiazenyl benzothiazole for in vivo imaging of neurofibrillary tangles in Alzheimer's disease brains, ACS Medicinal Chemistry Letters 3 (2012) 58–62.
[14] L.E. Rojo, J. Alzate-Morales, I.N. Saavedra, P. Davies, R.B. Maccioni, Selective interaction of lansoprazole and astemizole with tau polymers: potential new clinical use in diagnosis of Alzheimer's disease, Journal of Alzheimer's Disease 19 (2010) 573–589.
[15] L. Cai, R.B. Innis, V.W. Pike, Radioligand development for PET imaging of β-amyloid (Aβ)—current status, Current Medicinal Chemistry 14 (2007) 19–52.
[16] R. Leuma Yona, S. Mazeres, P. Faller, E. Gras, Thioflavin derivatives as markers for amyloid-β fibrils: insights into structural features important for high-affinity binding, ChemMedChem 3 (2008) 63–66.
[17] K. Cisek, J. Kuret, QSAR studies for prediction of cross-beta sheet aggregate binding affinity and selectivity, Bioorganic & Medicinal Chemistry 20 (2012) 1434–1441.
[18] S.R. Marder, J.E. Sohn, G.D. Stucky, Materials for Nonlinear Optics: Chemical Perspectives, American Chemical Society, Washington, DC, 1991.
[19] J.R. Jensen, K. Cisek, N.S. Honson, J. Kuret, Ligand polarizability contributes to tau fibril binding affinity, Bioorganic & Medicinal Chemistry 19 (2011) 5147–5154.
[20] N.S. Honson, J.R. Jensen, A. Abraha, G.F. Hall, J. Kuret, Small-molecule mediated neuroprotection in an in situ model of tauopathy, Neurotoxicity Research 15 (2009) 274–283.
[21] Z.P. Zhuang, M.P. Kung, C. Hou, D.M. Skovronsky, T.L. Gur, K. Plossl, J.Q. Trojanowski, V.M. Lee, H.F. Kung, Radioiodinated styrylbenzenes and thioflavins as probes for amyloid aggregates, Journal of Medicinal Chemistry 44 (2001) 1905–1914.
[22] G. Carmel, B. Leichus, X. Cheng, S.D. Patterson, U. Mirza, B.T. Chait, J. Kuret, Expression, purification, crystallization, and preliminary x-ray analysis of casein kinase-1 from *Schizosaccharomyces pombe*, Journal of Biological Chemistry 269 (1994) 7304–7309.
[23] M. Necula, C.N. Chirita, J. Kuret, Rapid anionic micelle-mediated α-synuclein fibrillization in vitro, Journal of Biological Chemistry 278 (2003) 46674–46680.
[24] E. Chang, J. Kuret, Detection and quantification of tau aggregation using a membrane filter assay, Analytical Biochemistry 373 (2008) 330–336.
[25] M. Goedert, R. Jakes, Expression of separate isoforms of human tau protein: correlation with the tau pattern in brain and effects on tubulin polymerization, EMBO Journal 9 (1990) 4225–4230.
[26] M. Hong, V. Zhukareva, V. Vogelsberg-Ragaglia, Z. Wszolek, L. Reed, B.I. Miller, D.H. Geschwind, T.D. Bird, D. McKeel, A. Goate, J.C. Morris, K.C. Wilhelmsen, G.D. Schellenberg, J.Q. Trojanowski, V.M. Lee, Mutation-specific functional impairments in distinct tau isoforms of hereditary FTDP-17, Science 282 (1998) 1914–1917.
[27] M. Necula, J. Kuret, Electron microscopy as a quantitative method for investigating tau fibrillization, Analytical Biochemistry 329 (2004) 238–246.
[28] W.E. Klunk, M.L. Debnath, J.W. Pettegrew, Development of small molecule probes for the beta-amyloid protein of Alzheimer's disease, Neurobiology of Aging 15 (1994) 691–698.
[29] M. Necula, C.N. Chirita, J. Kuret, Cyanine dye n744 inhibits tau fibrillization by blocking filament extension: implications for the treatment of tauopathic neurodegenerative diseases, Biochemistry 44 (2005) 10227–10237.
[30] M.J.e.a. Frisch, Gaussian 09, Gaussian, Inc. Revision A.1 (2009).
[31] R. Ahlrichs, M. Bar, M. Haser, H. Horn, C. Kolmel, Electronic-structure calculations on workstation computers—the program system turbomole, Chemical Physics Letters 162 (1989) 165–169.

[32] D. Jacquemin, E.A. Perpete, I. Ciofini, C. Adamo, Accurate simulation of optical properties in dyes, Accounts of Chemical Research 42 (2009) 326–334.
[33] C.M. Breneman, K.B. Wiberg, Determining atom-centered monopoles from molecular electrostatic potentials—the need for high sampling density in formamide conformational-analysis, Journal of Computational Chemistry 11 (1990) 361–373.
[34] J. Tomasi, B. Mennucci, R. Cammi, Quantum mechanical continuum solvation models, Chemical Reviews 105 (2005) 2999–3093.
[35] E.F. Pettersen, T.D. Goddard, C.C. Huang, G.S. Couch, D.M. Greenblatt, E.C. Meng, T.E. Ferrin, UCSF chimera—a visualization system for exploratory research and analysis, Journal of Computational Chemistry 25 (2004) 1605–1612.
[36] C.N. Chirita, J. Kuret, Evidence for an intermediate in tau filament formation, Biochemistry 43 (2004) 1704–1714.
[37] G. Kelenyi, On the histochemistry of azo group-free thiazole dyes, Journal of Histochemistry and Cytochemistry 15 (1967) 172–180.
[38] M.E. King, V. Ahuja, L.I. Binder, J. Kuret, Ligand-dependent tau filament formation: implications for Alzheimer's disease progression, Biochemistry 38 (1999) 14851–14859.
[39] M.P. Kung, D.M. Skovronsky, C. Hou, Z.P. Zhuang, T.L. Gur, B. Zhang, J.Q. Trojanowski, V.M. Lee, H.F. Kung, Detection of amyloid plaques by radioligands for Aβ40 and Aβ42: potential imaging agents in Alzheimer's patients, Journal of Molecular Neuroscience 20 (2003) 15–24.
[40] P. Friedhoff, A. Schneider, E.M. Mandelkow, E. Mandelkow, Rapid assembly of Alzheimer-like paired helical filaments from microtubule-associated protein tau monitored by fluorescence in solution, Biochemistry 37 (1998) 10223–10230.
[41] S.K. Saha, P. Purkayastha, A.B. Das, S. Dhara, Excited state isomerization and effect of viscosity- and temperature-dependent torsional relaxation on TICT fluorescence of trans-2-[4-(dimethylamino)styryl]benzothiazole, Journal of Photochemistry and Photobiology A: Chemistry 199 (2008) 179–187.
[42] F.A.S. Chipem, S. Chatterjee, G. Krishnamoorthy, Theoretical study on photochemical behavior of trans-2-[4′-(dimethylamino)styryl]benzothiazole, Journal of Photochemistry and Photobiology A: Chemistry 214 (2010) 121–127.
[43] J. Bieschke, M. Herbst, T. Wiglenda, R.P. Friedrich, A. Boeddrich, F. Schiele, D. Kleckers, J.M. Lopez del Amo, B.A. Gruning, Q. Wang, M.R. Schmidt, R. Lurz, R. Anwyl, S. Schnoegl, M. Fandrich, R.F. Frank, B. Reif, S. Gunther, D.M. Walsh, E.E. Wanker, Small-molecule conversion of toxic oligomers to nontoxic beta-sheet-rich amyloid fibrils, Nature Chemical Biology 8 (2012) 93–101.
[44] C. Rodriguez-Rodriguez, A. Rimola, L. Rodriguez-Santiago, P. Ugliengo, A. Alvarez-Larena, H. Gutierrez-de-Teran, M. Sodupe, P. Gonzalez-Duarte, Crystal structure of thioflavin-T and its binding to amyloid fibrils: insights at the molecular level, Chemical Communications 46 (2010) 1156–1158.
[45] C. Wu, M. Biancalana, S. Koide, J.E. Shea, Binding modes of thioflavin-T to the single-layer beta-sheet of the peptide self-assembly mimics, Journal of Molecular Biology 394 (2009) 627–633.
[46] C. Wu, M.T. Bowers, J.E. Shea, On the origin of the stronger binding of PIB over thioflavin T to protofibrils of the Alzheimer amyloid-β peptide: a molecular dynamics study, Biophysical Journal 100 (2011) 1316–1324.
[47] C. Wu, Z. Wang, H. Lei, Y. Duan, M.T. Bowers, J.E. Shea, The binding of thioflavin T and its neutral analog BTA-1 to protofibrils of the Alzheimer's disease $A\beta_{16-22}$ peptide probed by molecular dynamics simulations, Journal of Molecular Biology 384 (2008) 718–729.
[48] E.A. Meyer, R.K. Castellano, F. Diederich, Interactions with aromatic rings in chemical and biological recognition, Angewandte Chemie (International Ed. in English) 42 (2003) 1210–1250.
[49] J.R. Jensen, K. Cisek, K.E. Funk, S. Naphade, K. Schafer, J. Kuret, Research towards tau imaging, Journal of Alzheimer's Disease 26 (S3) (2011) 147–157.
[50] N.S. Honson, J. Kuret, Tau aggregation and toxicity in tauopathic neurodegenerative diseases, Journal of Alzheimer's Disease 14 (2008) 417–422.
[51] M. Novak, J. Kabat, C.M. Wischik, Molecular characterization of the minimal protease resistant tau unit of the Alzheimer's disease paired helical filament, EMBO Journal 12 (1993) 365–370.
[52] National Center for Biotechnology Information. PubChem Compound Database; CID=415676, http://pubchem.ncbi.nlm.nih.gov/summary/summary.cgi?cid=415676 (accessed May. 1, 2012).